**Showcasing research from the Laboratory of Molecular Structure and Dynamics, Institute of Chemistry, Eötvös Loránd University, Budapest, Hungary**

Title: Rovibrational transitions of the methane−water dimer from intermolecular quantum dynamical computations

Quantum dynamical computations of the weakly bound, highly fluxional methane−water dimer explain high-resolution far-infrared spectroscopic measurements and validate the intermolecular model potentials of this prototype of the water hydrocarbon interactions.
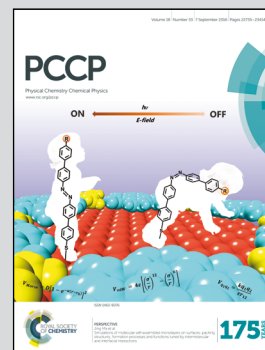
ROYAL SOCIETY
OF **CHEMISTRY**

www.rsc.org/pccp

Registered charity number: 207890

PCCP

Rovibrational transitions of the methane–water dimer from intermolecular quantum dynamical computations†

János Sarka,[ab] Attila G. Császár,[ab] Stuart C. Althorpe,[c] David J. Wales[c] and Edit Mátyus*[a]

Rovibrational quantum nuclear motion computations, with $J = 0$, 1, and 2, are reported for the intermolecular degrees of freedom of the methane–water dimer, where J is the quantum number describing the overall rotation of the complex. The computations provide the first explanation of the far-infrared spectrum of this complex published in *J. Chem. Phys.*, 1994, **100**, 863. All experimentally reported rovibrational transitions, up to $J = 2$, can be assigned to transitions between the theoretically computed levels. The deviation of the experimental and computed rovibrational transitions is 0.5 cm^{-1} for the *ortho* and 2 cm^{-1} for the *para* species with a variance of 0.005 cm^{-1}. In addition to a lower systematic error, the overall agreement of theory and experiment is also better for the *ortho* species (involving *ortho*-H_2O). Most importantly, for this species all levels of the 24-fold tunneling splitting manifold corresponding to the zero-point vibration (ZPV) are involved in at least one experimentally reported transition. For the *para* species there are a few energy levels in the computed ZPV manifold that are not involved in the reported experimental transitions. Furthermore, computed energy levels are identified that correspond to the ZPV tunneling splitting manifold of the secondary minimum structure of the dimer, which presumably appear in rovibrational transitions in the same energy regime as the observed transitions, but have not been experimentally reported.

1 Introduction

A molecular-level representation of materials by an *ab initio* potential energy surface (PES) can be used to make reliable predictions about bulk-phase properties, relevant from biological simulations to technological applications. A universal PES, which can be used from the monomers through the dimer, trimer, *etc.* to the bulk phase, relies on an incremental *n*-body expansion, and usually consists of only the monomer PESs, the dimer interaction energy, and the trimer interaction energy contributions.[1–7] Exact quantum dynamical computations of clusters map this PES representation onto transitions between rotational and vibrational energy levels—directly measurable quantities by spectroscopic techniques to high precision. This spectroscopic validation, through the direct comparison of the computed and measured rovibrational

transition energies of the dimer, trimer, and larger clusters, provides a stringent test of this incremental representation of materials.

Complexes of methane and water are important for gas storage, including the naturally captured methane in marine and arctic reservoirs,[8] and transportation. The infrared spectrum of methane clathrate hydrate has been reported in ref. 9 and might find significant astrophysical applications. Recent local-monomer, vibrational self-consistent field, and virtual-state configuration interaction theory computations of $CH_4@(H_2O)_{20}$[10] show good agreement with the experimental Raman spectrum recorded in the C–H stretch region.[11,12] The methane–water dimer has been studied at high resolution in the microwave[13] and the far-infrared[14] regions of the spectrum; however, a detailed theoretical quantum dynamical characterization of this simplest complex has never been carried out.

The quantum dynamical description of $CH_4 \cdot H_2O$ is challenging because all intermolecular degrees of freedom correspond to highly delocalized motions, resulting from the fluxional and loosely bound character of the complex. These 'difficult' fluxional degrees of freedom play a central role in binding the water and methane molecules. Hence, an exact quantum mechanical description of (at least) the intermolecular degrees of freedom

[a] Institute of Chemistry, Eötvös Loránd University, Pázmány Péter sétány 1/A, H-1117 Budapest, Hungary. E-mail: matyus@chem.elte.hu

[b] MTA-ELTE Complex Chemical Systems Research Group, Eötvös Loránd University, P.O. Box 32, H-1518 Budapest 112, Hungary

[c] Department of Chemistry, University of Cambridge, Lensfield Road, Cambridge, CB2 1EW, UK

† Electronic supplementary information (ESI) available. See DOI: 10.1039/c6cp03062a

is necessary to validate the intermolecular potential energy surface (PES). Such a validation is important for the construction of a universal PES for the $(CH_4)_n@(H_2O)_m$ systems.

In the present article, we describe the direct numerical solution of the rovibrational Schrödinger equation for the dimer with rigid monomers using the *ab initio* PES of ref. 15 (and also report preliminary computations performed with the PES of ref. 6). The computed rovibrational transitions are compared with far-infrared (FIR) spectroscopic measurements.[14] This comparison allows us to directly test the accuracy of the PES representations of the methane–water bimolecular interactions. Understanding the transitions seen in the FIR measurements not only requires the application of the best present-day quantum dynamics techniques pushed to their technical limits, but also the development of several tools for the detailed analysis of the results obtained.

In Section 2, we define the rovibrational Hamiltonian used in this study and explain the details of the numerical solution of the corresponding Schrödinger equation. Section 3.1 lists a few relevant results about the PES of the dimer and Section 3.2 is a summary of the symmetry analysis, provided in full detail in the ESI,† which is followed by the presentation and discussion of the computed vibrational energy levels, rovibrational energy levels, and rovibrational transitions in Sections 3.3, 3.4, and 3.5, respectively. The article ends with Section 4, containing a summary and the most important conclusions.

2 Numerical solution of the rovibrational Schrödinger equation of the intermolecular degrees of freedom

We have carried out a numerical study of the intermolecular degrees of freedom of the methane–water dimer using the rovibrational quantum dynamics computer program GENIUSH,[16,17] and related wave function analysis tools.[18,19] The program and the related methodology have been used before for a number of floppy,[16,17,20] fluxional,[21] and astructural[19,22] molecules and complexes. In what follows, we summarize the theoretical background and specify the computational parameters used during the present study.

The methane–water complex includes $N = 8$ atomic nuclei and we describe the intermolecular dynamics by considering $D = 6$ active degrees of freedom (Fig. 1). The general rovibrational Hamiltonian implemented in GENIUSH[16,17] is

$$
\begin{aligned}
\hat{H} = &\frac{1}{2}\sum_{k=1}^{D}\sum_{l=1}^{D}\tilde{g}^{-1/4}\hat{p}_k G_{kl}\tilde{g}^{1/2}\hat{p}_l\tilde{g}^{-1/4} \\
&+\frac{1}{2}\sum_{k=1}^{D}\sum_{a=1}^{3}\left(\hat{p}_k G_{k,D+a} + G_{k,D+a}\hat{p}_k\right)\hat{J}_a \\
&+\frac{1}{2}\sum_{a=1}^{3}G_{D+a,D+a}\hat{J}_a^2 \\
&+\frac{1}{2}\sum_{a=1}^{3}\sum_{b>a}^{3}G_{D+a,D+b}\left(\hat{J}_a\hat{J}_b + \hat{J}_b\hat{J}_a\right) + \hat{V},
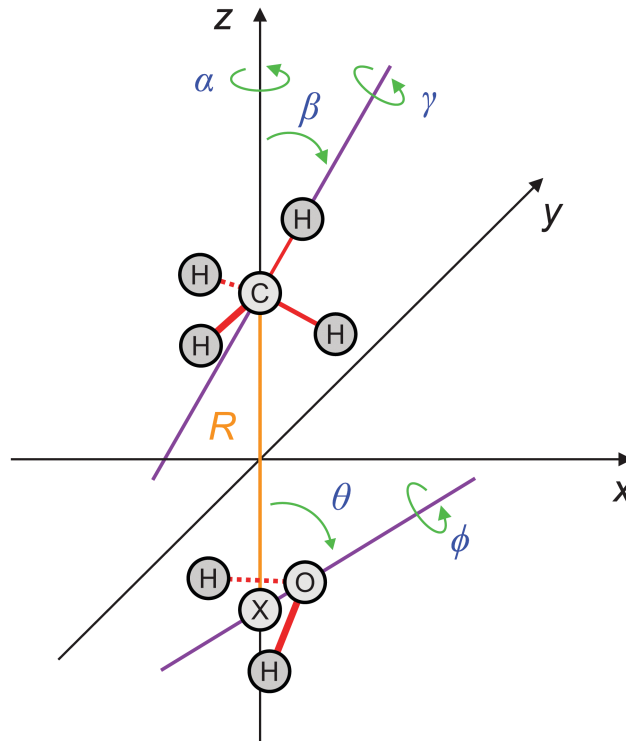\end{aligned}
\tag{1}
$$

Fig. 1 Internal coordinates $(R,\theta,\phi,\alpha,\beta,\gamma)$ and the body-fixed frame (x, y, z) employed in the rovibrational computations restricted to intermolecular motions. X labels the center of mass of the water molecule.

where the operators $\hat{p}_k = -i\partial/\partial q_k$ (in atomic units) correspond to the q_k ($k = 1, 2,\ldots,D$) internal coordinates and $\hat{J}_a$ ($a = 1(x), 2(y), 3(z)$) are the body-fixed angular momentum operators. The coefficients, $G_{kl} = (\mathbf{g}^{(inter)})_{kl}^{-1}$ and $\tilde{g} = \det(\mathbf{g}^{(inter)})$, are obtained from the reduced-dimensional $\mathbf{g}$ matrix (which depends also on the structure of the constrained moieties)

$$
g_{kl}^{(inter)} = \sum_{i=1}^{N} m_i \mathbf{t}_{ik}^{T}\mathbf{t}_{il}, \quad k,l = 1, 2,\ldots, D + 3
\tag{2}
$$

with

$$
\mathbf{t}_{ik} = \frac{\partial \mathbf{r}_i}{\partial q_k}, \quad k = 1, 2,\ldots, D
\tag{3}
$$

$$
\mathbf{t}_{i,D+a} = \mathbf{e}_a \times \mathbf{r}_i, \quad a = 1(x), 2(y), 3(z)
\tag{4}
$$

evaluated for the body-fixed Cartesian coordinates, $\mathbf{r}_i$, and the unit vectors, $\mathbf{e}_a$, of the body-fixed frame. The volume element corresponding to the Hamiltonian, eqn (1), is $dV = dq_1 dq_2\ldots dq_D d\alpha_1 d\alpha_2 d\alpha_3$. This intermolecular (reduced-dimensional) quantum Hamiltonian rigorously accounts for the geometrical constraint of the monomer structures for fixed reference geometries, since it is obtained from the classical Lagrangian in which the time derivatives of the monomer structural parameters are set to zero.[16]

The six active internal coordinates visualized in Fig. 1 are defined as follows: the distance of the center-of-mass of the two molecules, $q_1 = R \in [0,\infty)$, angles of the spherical polar coordinates $\rho = (\theta,\phi)$ of H_2O, $q_2 = \cos\theta \in [-1,1]$, $q_3 = \phi \in [0,2\pi)$, and the Euler angles for CH_4, (α,β,γ) with $q_4 = \alpha \in [0,2\pi)$,

This journal is © the Owner Societies 2016

Phys. Chem. Chem. Phys., 2016, **18**, 22816–22826 | **22817**

$q_5 = \cos\beta \in [-1,1]$, and $q_6 = \gamma \in [0,2\pi]$. The z axis of the right-handed (x,y,z) body-fixed frame is attached to the centers of mass of the two moieties and points from the water towards the methane subunit. We used the same monomer structures (effective ground-state vibrational structures) as in ref. 15, i.e., the fixed structure of the water molecule is defined by $r(\text{O–H})$ = 0.9716257 Å and $\alpha(\text{H–O–H})$ = 104.69°,[23] slightly different from the vibrationally averaged parameters two of us computed before,[24] $\langle r_{\text{OH}}\rangle$ = 0.97565 Å and $\langle\alpha_{\text{HOH}}\rangle$ = 104.43°. The fixed structure of the methane molecule is a regular tetrahedron, $\cos\alpha(\text{H–C–H})$ = $-1/3$, with $r(\text{C–H})$ = 1.099122 Å.[15,25] We used $m(\text{H})$ = 1.007825 u, $m(\text{C})$ = 12 u, and $m(\text{O})$ = 15.994915 u masses for the atomic nuclei, and the following conversion factors among the different energy units:[26] $1E_h$ = 219474.63 cm^{-1} = 627.5095 kcal mol^{-1}, and 1 MHz = 3.335641 × 10^{-5} cm^{-1} (the PES of ref. 15 is available in kcal mol^{-1} units, we use atomic units during the variational computation, and the experimental results are available in MHz).

In the GENIUSH code the matrix representation of the Hamiltonian is constructed using the discrete variable representation (DVR) for the vibrational degrees of freedom along with symmetrized Wang functions for the rotational degrees of freedom. Table 1 summarizes the parameters of the computations. With these parameters the energy levels (and degeneracies) could be converged to within around 0.05 cm^{-1}. The computed energy-level lists for J = 0, 1, and 2 obtained with the AOSz05 PES[15] (the zero of the energy scale is shifted to the energy of the global minimum) are included in the ESI.† In the article we refer to these energy levels with the unambiguous labels J0.n, J1.n, and J2.n for J = 0, 1, and 2, respectively, where n = 1, 2,... is an integer that enumerates the energy levels based on their energy order. Tighter convergence (within ∼0.005 cm^{-1}) of the degenerate levels can be obtained by using unscaled Legendre DVR points for the $q_5 = \cos\beta$ degree of freedom; however, a 3–5 times larger grid and about 10 times more CPU are required compared with the computations specified in Table 1.

We have also tested the performance of the more recent PES of ref. 6. The agreement of the vibrational energy levels computed up to ca. 65 cm^{-1} with the two PESs[6,15] is better than 1.5 cm^{-1} and for several levels it 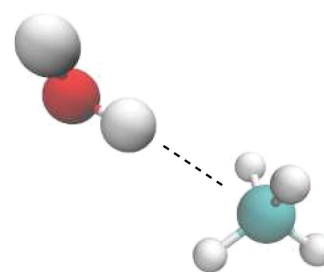is better than 0.2 cm^{-1}. This is a very reassuring result for the two PESs and the accuracy of the present rovibrational computations. We now present and discuss in detail the results obtained with the AOSz05 PES. (For comparison, the vibrational (J = 0) energy levels obtained with both PESs[6,15] and with both the scaled and the unscaled Legendre DVR grids are included in the ESI.†)
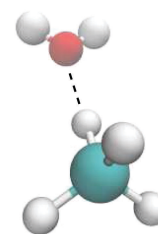
3 Discussion of the numerical results

This section presents the most relevant properties of the PES (Section 3.1), a short summary of the symmetry analysis of the dimer (Section 3.2), and a detailed discussion of the numerical results of the quantum dynamical computations including the computed vibrational energy levels (Section 3.3), the computed rovibrational energy levels (Section 3.4), and a comparison of the computed and experimental rovibrational transitions and theoretical predictions for further possible experimental observations (Section 3.5).

3.1 Minima on the AOSz05 PES

The electronic ground-state PES of the methane–water dimer supports two local minima (see Fig. 2 and Table 1), both of C_s point group symmetry. The secondary minimum (SM) is 99 cm^{-1} higher in energy than the global minimum (GM) on the AOSz05 potential energy surface.[15] (The minimum-energy pathway located with OPTIM[27,28] on this PES connecting the global and the secondary minimum structures is shown in Fig. S3 of the ESI.†) In the GM the water molecule is the proton donor, while in the SM the water molecule behaves as an acceptor.

(a) Global minimum (GM)

(b) Secondary minimum (SM)

Fig. 2 Equilibrium structures of the AOSz05 potential energy surface.[15] The secondary minimum (SM) is 99 cm^{-1} higher in energy than the global minimum (GM).

Table 1 Internal coordinates (Coord.), discrete variable representations (DVR), number of grid points (N), and grid intervals employed during the final variational computations carried out using the GENIUSH code

Coord.	GM[a]	SM[a]	Nuclear motion computations		
			DVR type[b]	N	Grid interval
R [Å]	3.464	3.773	PO Laguerre DVR	15	Scaled to [2.5,6.0]
θ [°]	116.19	22.15[c]	PO Legendre DVR	14	Scaled to [1,179]
ϕ [°]	90.00	0.00	Exponential DVR	15	Unscaled on [0,360]
α [°]	297.46	299.78	Exponential DVR	9	Unscaled on [0,360]
β [°]	113.05	70.17	PO Legendre DVR	21	Scaled to [1,179]
γ [°]	293.01	240.66	Exponential DVR	21	Unscaled on [0,360]

[a] The values of the internal coordinates are provided for the global minimum (GM) and for the secondary minimum (SM) structures of the AOSz05 PES.[15] [b] PO: potential-optimized DVR, i.e., subsequent optimization of the DVR points with a one-dimensional model. [c] The PES is relatively flat along the θ coordinate in the SM well.

3.2 Symmetry analysis

The feasible permutation-inversion operations of the dimer belong to the G_{48} molecular symmetry (MS) group.[14] A detailed symmetry analysis, very similar to Dyke's analysis for the water dimer,[29] as well as the character table of G_{48} are provided in the ESI.† The GM (and also the SM) structure of the underlying PES has C_s point group symmetry; thus, the dimer has only 24 (instead of 48) distinct, rotationally non-superimposable structures. Therefore (see the ESI†) the zero-point vibration (ZPV) with $J = 0$ (or any other totally symmetric state) splits into 24 levels, see eqn (S1) (ESI†), characterized by the following symmetry species:

$$\Gamma(\text{ZPV}, J = 0) = A_1^+ \oplus E^+ \oplus F_1^+ \oplus 2F_2^+ \oplus A_2^- \oplus E^- \oplus 2F_1^- \oplus F_2^-. \tag{5}$$

The + and − superscripts of the irreps differentiate between the symmetric and antisymmetric character of the wave function with respect to the exchange of the two protons of the water molecule. To obtain a total spin-spatial wave function that is antisymmetric with respect to proton exchange, the (+) states have to be combined with the *para* spin function, $[\alpha(1)\beta(2) - \beta(1)\alpha(2)]/\sqrt{2}$, while the (−) states have to be combined with one of the *ortho* spin functions, $\{\alpha(1)\alpha(2), \beta(1)\beta(2), [\alpha(1)\beta(2) + \beta(1)\alpha(2)]/\sqrt{2}\}$. Hence, we use (+) and *para* or (−) and *ortho* interchangeably.

3.3 Vibrational energy levels

Vibrational energy levels computed using the GENIUSH code are visualized at the left of Fig. 3. At the right of the figure we provide the symmetry labels and a qualitative description of the levels up to *ca.* 65 cm^{-1}, based on the analysis of the wavefunctions.

The splitting manifold of the ZPV spans 36.4 cm^{-1} and separates into a 'lower' and an 'upper' part. The levels can be distinguished by the 'ortho' and 'para' spin states of the water molecule. The upper-lower separation is $\Delta_o^{\text{ul}} = 23.5$ cm^{-1} for the *ortho* and $\Delta_p^{\text{ul}} = 29.8$ cm^{-1} for the *para* species. (Δ is the difference between the centers of the 'upper' and the 'lower' levels calculated as the degeneracy-weighted average of the corresponding energies.) The large upper-lower separation can be understood in terms of the extremely facile internal rotation of the CH$_4$ moiety around the O–H$\cdots$H$_3$C–H hydrogen bond (Fig. 2), which is apparently slightly more hindered for the *ortho* species. The three-fold symmetry of the methane internal rotation,[30] and the corresponding A $\oplus$ E irreducible decomposition within the C_3 symmetry group, explains the 1:2 ratio of the number of levels in the lower and upper parts of the splitting pattern. The lower part covers a range of 11.2 cm^{-1} and includes the 'para' A$_1^+$ and F$_1^+$ and the 'ortho' A$_2^-$ and F$_2^-$ species. The *ortho–para* separation of the degeneracy-weighted average in this lower part is $\Delta_{op}^l = 6.5$ cm^{-1}. Interestingly, the same *ortho–para* separation in the upper part of the ZPV manifold is much smaller, only $\Delta_{op}^u = 0.2$ cm^{-1}. In general, the upper part is more congested and overlaps with a totally symmetric level that does not fit in this ZPV manifold, since eqn (5) tells us that the ZPV manifold accommodates only a single totally symmetric state. The DVR plots of this 'intruder'
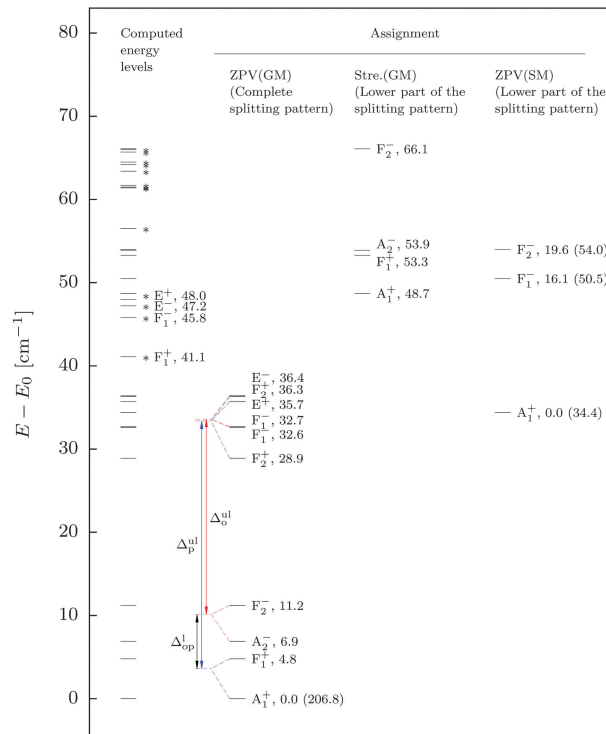

Fig. 3 Vibrational energy levels obtained using the GENIUSH code for the intermolecular degrees of freedom (with rigid monomers). The computed energy levels are shown at the left of the figure, and the symmetry species and characterization are provided at the right, except for those levels labeled with * (which are left unassigned for the present work). The global minimum (GM) and secondary minimum (SM) structures are shown in Fig. 2. ZPV labels the zero-point vibrational manifold and Stre. stands for stretching fundamental of the intermolecular distance. Definition and discussion of the $\Delta_{op}^l = 6.5$ cm^{-1}, $\Delta_o^{\text{ul}} = 23.5$ cm^{-1}, and $\Delta_p^{\text{ul}} = 29.8$ cm^{-1} values are provided in the text.

state (J0.18, 34.4 cm^{-1}) are very similar to the plots of the ground state, whereas the expectation values of some structural parameters markedly differ from those of the ground state (see Fig. 4). Based on these observations we assign this level, as well as the J0.37–39 (50.5 cm^{-1}), the J0.44–46 (54.0 cm^{-1}), and the J0.56–57 (63.4 cm^{-1}) levels, to the zero-point vibrational splitting manifold of the secondary minimum structure, Fig. 2b. The SM has a very shallow potential energy well and accordingly the computed splitting pattern is more diffuse, and we have not attempted to identify all levels in the ZPV(SM).

As well as the ZPV manifolds of the global and the secondary minimum structures, we obtained many more energy levels beyond around 65 cm^{-1}. Besides the ZPV(GM) and a few levels from the ZPV(SM), we could unambiguously trace a few levels of the splitting manifold of the intermolecular stretching fundamental by identifying a nodal plane along the R coordinate in the DVR plots (selected examples are shown in the ESI†). The stretching fundamental vibration is totally symmetric, similar to the ZPV; therefore, the same symmetry species are present in this splitting manifold as in the ZPV manifold, eqn (5). We identified the 'lower part' of this stretching manifold, Stre. A$_1^+$ (48.7 cm^{-1}, J0.36), Stre. F$_1^+$ (53.3 cm^{-1}, J0.40–42), Stre. A$_2^-$

This journal is © the Owner Societies 2016

Phys. Chem. Chem. Phys., 2016, **18**, 22816–22826 | **22819**
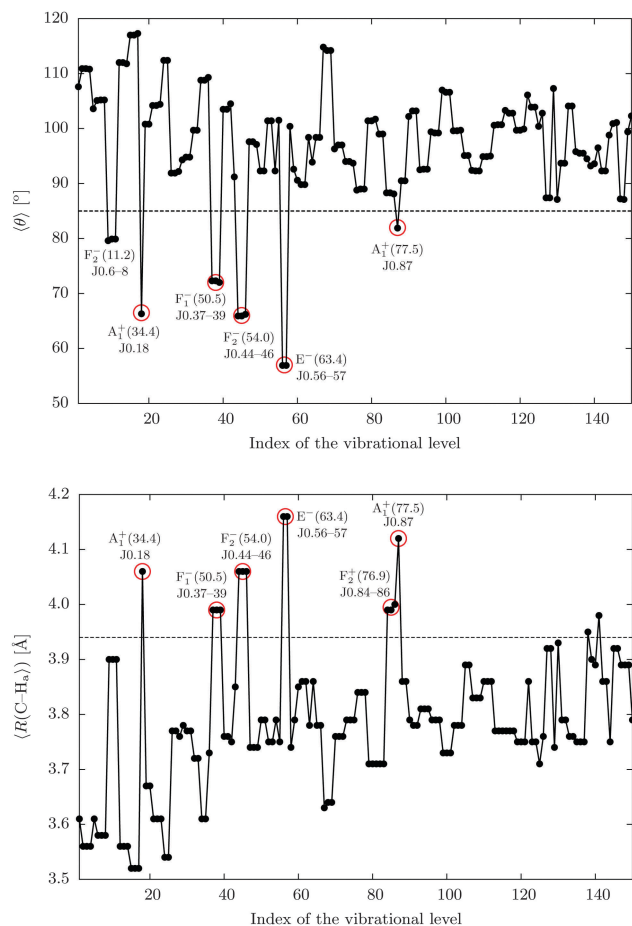
Fig. 4 Expectation values of structural parameters computed with the vibrational wave functions. θ is the tilt of H_2O and $R(C-H_a)$ measures the distance between the carbon nucleus of CH_4 and a hydrogen in H_2O (the exchange of the two hydrogens is feasible, and thus we obtain the same expectation value for both). These structural parameters have very different values in the equilibrium structures of the two minima (see Fig. 2), and this difference also appears (less markedly) in the expectation values. Vibrational levels that have been assigned to the secondary minimum, based on these structural differences, are highlighted with a red circle.

(53.9 cm^{-1}, J0.43), and Stre. F_2^- (66.1 cm^{-1}, J0.63,65,66). Indeed, Stre(GM) has a very similar structure to ZPV(GM) but it is characterized by a larger *ortho–para* separation, Δ_{op}^l(Stre) = 10.9 cm^{-1}, which might be explained by weaker interactions (and hence 'lower barriers') than in the zero-point energy state. The energy of the lowest-lying state of the stretching fundamental manifold is 48.7 cm^{-1}, only 12 cm^{-1} higher than the energy of the top level of the ZPV(GM) manifold. This is another clear indication of the very weakly bound character of this complex. There are levels that overlap or are even lower in energy than the 'lower' part of the stretching manifold, but left unassigned during the present work (and hence labeled with * at the left of Fig. 3). Some of these levels could be associated with the ZPV manifold of the secondary minimum and others might belong to some intermolecular bending vibrations. Beyond a certain energy range a conclusive separation of the computed levels between the global minimum well and the

secondary minimum well is probably not possible, because these minima have the same point group symmetry.

3.4 Rovibrational energy levels

The rotational constants corresponding to the GM structure, Fig. 2, are $A = 4.229$ cm^{-1}, $B = 0.159$ cm^{-1}, and $C = 0.158$ cm^{-1}, which indicate an almost perfect prolate symmetric top character. In addition, extremely strong rotational–vibrational mixing is anticipated due to the weak interaction between the two moieties.

The computed rovibrational energy levels with $J = 0$, 1, and 2, relevant to the experimental FIR observations,[14] are collected in Fig. 5 and 6 for the *ortho* and the *para* species, respectively. The (ro)vibrational bands in this figure are arranged similarly to Fig. 1 of the experimental paper.[14] A detailed, quantitative comparison of the computed and the experimental transitions is provided in the next subsection.

The most peculiar feature of the rovibrational energy-level manifold is the occasionally reversed ordering of the vibrational and rovibrational levels, *i.e.*, when a $J = 1$ rovibrational level is lower in energy than its parent vibrational energy level (a parent vibrational level is the dominant vibrational level provided by the rigid rotor decomposition (RRD) analysis of the rovibrational states[18]). This anomalous rovibrational ordering occurs within the F_2^+ (28.9 cm^{-1}, J0.9–11; 36.3 cm^{-1}, J0.21–23), E^+ (35.7 cm^{-1}, J0.19–20), F_1^- (32.6 cm^{-1}, J0.12–14; 32.7 cm^{-1}, J0.15–17), and E^- (36.4 cm^{-1}, J0.24–25) bands of the ZPV(GM), and each of these parent vibrational energy levels appear in the 'upper' part of the ZPV(GM) splitting manifold. The reversed statement is also true: all vibrational bands in the 'upper' part of the ZPV(GM) splitting manifold feature anomalous negative rotational 'excitation' energies. This behavior can be understood using the coupled rotors picture: by coupling the rotation of the (rigid) water molecule, the rotation of the (rigid) methane molecule, and the end-over-end rotation of the entire complex.[14,31] The evaluation of the overlap of the exact wave function with these coupled-rotor model functions (for various subsystem angular momenta) is left for future work, and will allow us to make a quantitative assignment to this coupled multiple-rotors model (which is another limiting model along with the common RR model). For the present work, to qualitatively highlight the explained ideas, we defined and constructed energy decomposition tables (see the ESI†), which show the energy contribution of the different terms (and hence different rotors) of the Hamiltonian to the variationally computed (ro)vibrational energy of the complex.

3.5 Rovibrational transitions

In addition to the rovibrational energy levels with $J = 0$, 1, and 2, Fig. 5 and 6 show the rovibrational transitions that could be identified in the experimental transitions reported in ref. 14. The transitions are labeled with 1,2,... in each band and the same label is used in the corresponding Tables 2–9. There are also experimental observations with higher J values, which could be explored *via* further computations; however, the results computed with $J = 0$, 1, and 2 already highlight the peculiar features (negative rotational excitation energies) of the rovibrational level structure, and also allow us to establish a firm, quantitative comparison
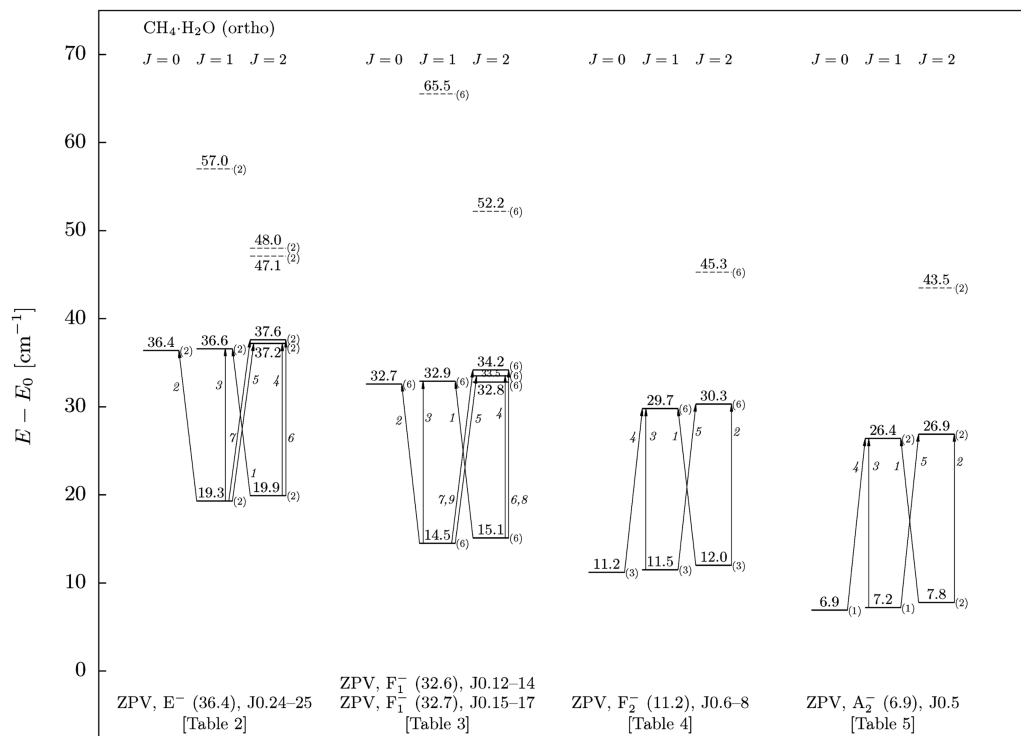
22820 | *Phys. Chem. Chem. Phys.*, 2016, **18**, 22816–22826

This journal is © the Owner Societies 2016

Fig. 5 Rovibrational energy levels, in cm^{-1}, and observed[14] and computed transitions of the CH$_4$·(*ortho*-H$_2$O) dimer with J = 0, 1, 2 (the numbers in italics label the transitions documented in the corresponding tables). The label (*n*) next to each line indicates the number of degenerate or near degenerate energy levels with the average energy given in the figure (rounded to the first decimal place). The dashed lines indicate strongly mixed states with small contributions from the ZPV species in which they are listed.
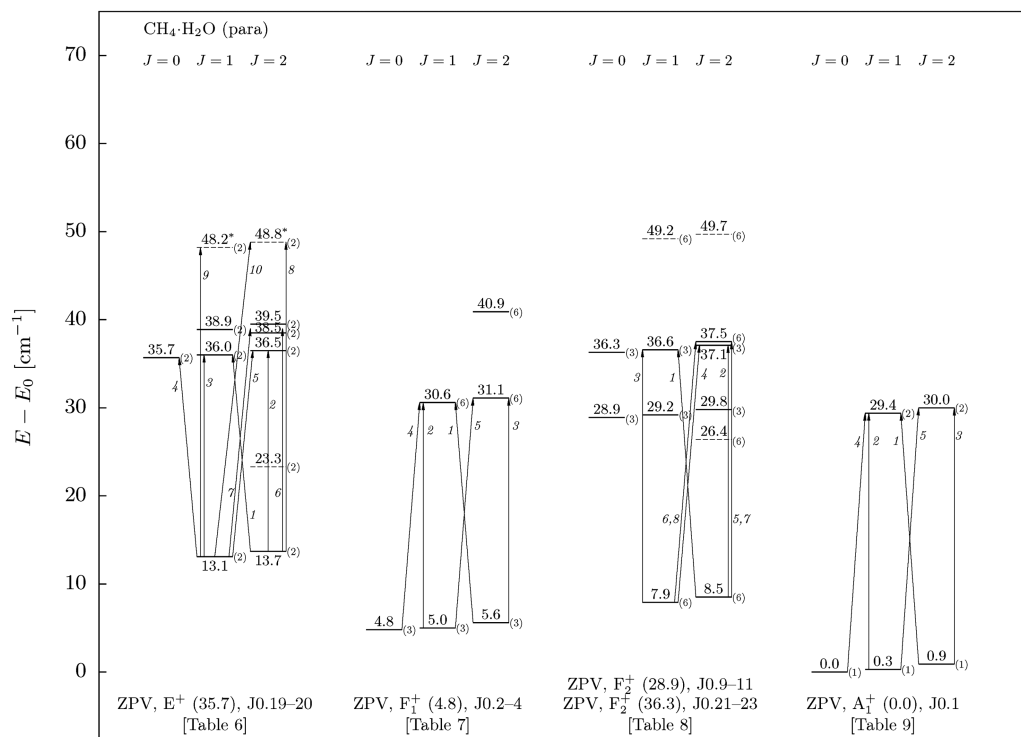
Fig. 6 Rovibrational energy levels, in cm^{-1}, and observed[14] and computed transitions of the CH$_4$·(*para*-H$_2$O) dimer with J = 0, 1, 2 (the numbers in italics identify the lines of the corresponding tables). The label (*n*) next to each line indicates the number of degenerate or near degenerate energy levels with the average energy given in the figure (rounded to the first decimal place). The levels labeled with * are assignable to the E$^+$ 48.2 cm^{-1} (J0.34−35) vibration. The dashed lines indicate strongly mixed states with small contributions from the ZPV species in which they are listed.

This journal is © the Owner Societies 2016

Phys. Chem. Chem. Phys., 2016, **18**, 22816−22826 | **22821**

with the experimental results, see Tables 2–9. (The computed rovibrational energy level list is provided in the ESI.†)

Evidently, the observed transitions take place within the rovibrational ZPV(GM) manifold with only three exceptions

Table 2 Rovibrational transitions assigned to the E^- 36.4 cm^{-1} (J0.24–25) level of the zero-point vibration

No.	$J' \leftarrow J''$	Expt [MHz]	Expt [cm^{-1}]	$E(J')$ [cm^{-1}]	Label $(J')^a$	$E(J'')$ [cm^{-1}]	Label $(J'')^a$	Calc. [cm^{-1}]	δ^b [cm^{-1}]
Expt. (ref. 14): Table III, E1, $\Sigma \leftarrow \Pi$ band									
1	$1 \leftarrow 2$	524254.1	17.5	36.6	J1.56–57	19.9	J2.23–24	16.8	0.7
2	$0 \leftarrow 1$	532812.0	17.8	36.4	J0.24–25	19.3	J1.23–24	17.0	0.7
3	$1 \leftarrow 1$	541359.5	18.1	36.6	J1.56–57	19.3	J1.23–24	17.3	0.7
4	$2 \leftarrow 2$	541344.3	18.1	37.2	J2.78–79	19.9	J2.23–24	17.3	0.7
5	$2 \leftarrow 1$	558451.2	18.6	37.2	J2.78–79	19.3	J1.23–24	17.9	0.7
Expt. (ref. 14): Table III, E2, $\Delta \leftarrow \Pi$ band									
6	$2 \leftarrow 2$	542744.8	18.1	37.6	J2.86	19.9	J2.23–24	17.7	0.4
7	$2 \leftarrow 1$	559850.8	18.7	37.6	J2.86	19.3	J1.23–24	18.2	0.4

^{a} J$n.i$–j identifies the levels in the energy-level list provided in the ESI. ^{b} δ is the difference of the experimental and computed transitions. The mean and the sample variance of the deviation in the E1 and E2 bands are $(\bar{\delta},\sigma_\delta) = (0.7,0.002)$ cm^{-1} and $(0.4,0.003)$ cm^{-1}, respectively.

Table 3 Rovibrational transitions assigned to the F_1^- 32.6 cm^{-1} (J0.12–14) and 32.7 cm^{-1} (J0.15–17) levels of the zero-point vibration

No.	$J' \leftarrow J''$	Expt [MHz]	Expt [cm^{-1}]	$E(J')$ [cm^{-1}]	Label $(J')^a$	$E(J'')$ [cm^{-1}]	Label $(J'')^a$	Calc. [cm^{-1}]	δ^b [cm^{-1}]
Expt. (ref. 14): Table IV, (A/F)1, $\Sigma \leftarrow \Pi$ band									
1	$1 \leftarrow 2$	529495.8	17.7	32.9	J1.44–49	15.1	J2.17–22	17.8	−0.2
2	$0 \leftarrow 1$	538189.8	18.0	32.7	J0.12–17	14.5	J1.17–22	18.1	−0.2
3	$1 \leftarrow 1$	546831.5	18.2	32.9	J1.44–49	14.5	J1.17–22	18.4	−0.2
4	$2 \leftarrow 2$	546715.2	18.2	33.5	J2.60–65	15.1	J2.17–22	18.4	−0.2
5	$2 \leftarrow 1$	564291.7	18.8	33.5	J2.60–65	14.5	J1.17–22	19.0	−0.1
Expt. (ref. 14): Table IV, (A/F)3a, $\Delta \leftarrow \Pi$ band									
6	$2 \leftarrow 2$	564637.3	18.8	34.2	J2.66–71	15.1	J2.17–22	19.1	−0.2
7	$2 \leftarrow 1$	581971.4	19.4	34.2	J2.66–71	14.5	J1.17–22	19.6	−0.2
Expt. (ref. 14): Table IV, (A/F)3b, $\Delta \leftarrow \Pi$ band									
8	$2 \leftarrow 2$	564437.7	18.8	34.2	J2.66–71	15.1	J2.17–22	19.1	−0.2
9	$2 \leftarrow 1$	582013.5	19.4	34.2	J2.66–71	14.5	J1.17–22	19.6	−0.2

^{a} J$n.i$–j identifies the levels in the energy level list provided in the ESI. ^{b} δ is the difference between the experimental and computed transitions. The mean and the sample variance of the deviation in the (A/F)1, (A/F)3a, and (A/F)3b bands are $(\bar{\delta},\sigma_\delta) = (-0.2,0.002)$ cm^{-1}, $(-0.2,0.001)$ cm^{-1}, and $(-0.2,0.005)$ cm^{-1}, respectively.

Table 4 Rovibrational transitions assigned to the F_2^- 11.2 cm^{-1} (J0.6−8) level of the zero-point vibration

No.	$J' \leftarrow J''$	Expt [MHz]	Expt [cm^{-1}]	$E(J')$ [cm^{-1}]	Label $(J')^a$	$E(J'')$ [cm^{-1}]	Label $(J'')^a$	Calc. [cm^{-1}]	δ^b [cm^{-1}]
Expt. (ref. 14): Table V, (A/F)2, $\Pi \leftarrow \Sigma$ band									
1	$1 \leftarrow 2$	536931.0	17.9	29.8	J1.32–37	12.0	J2.12–14	17.7	0.2
2	$2 \leftarrow 2$	553883.6	18.5	30.3	J2.42–47	12.0	J2.12–14	18.3	0.2
3	$1 \leftarrow 1$	553888.4	18.5	29.8	J1.32–37	11.5	J1.12–14	18.3	0.2
4	$1 \leftarrow 0$	562445.5	18.8	29.8	J1.32–37	11.2	J0.6–8	18.6	0.2
5	$2 \leftarrow 1$	571055.5	19.0	30.3	J2.42–47	11.5	J1.12–14	18.9	0.2

^{a} J$n.i$–j identifies the levels in the energy-level list provided in the ESI. ^{b} δ is the difference of the experimental and computed transitions. The mean and the sample variance of the deviation are $(\bar{\delta},\sigma_\delta) = (0.2,0.004)$ cm^{-1}.

Table 5 Rovibrational transitions assigned to the A_2^- 6.9 cm^{-1} (J0.5) level of the zero-point vibration

No.	$J' \leftarrow J''$	Expt [MHz]	Expt [cm^{-1}]	$E(J')$ [cm^{-1}]	Label $(J')^a$	$E(J'')$ [cm^{-1}]	Label $(J'')^a$	Calc. [cm^{-1}]	δ^b [cm^{-1}]
Expt. (ref. 14): Table VI, (A/F)4, $\Pi \leftarrow \Sigma$ band									
1	$1 \leftarrow 2$	548506.7	18.3	26.4	J1.25–26	7.8	J2.5	18.6	−0.3
2	$2 \leftarrow 2$	565694.1	18.9	26.9	J2.33–34	7.8	J2.5	19.1	−0.3
3	$1 \leftarrow 1$	565694.1	18.9	26.4	J1.25–26	7.2	J1.5	19.1	−0.3
4	$1 \leftarrow 0$	574574.9	19.2	26.4	J1.25–26	6.9	J0.5	19.4	−0.3
5	$2 \leftarrow 1$	583344.0	19.5	26.9	J2.33–34	7.2	J1.5	19.7	−0.3

^{a} J$n.i$–j identifies the levels in the energy-level list provided in the ESI. ^{b} δ is the difference of the experimental and computed transitions. The mean and the sample variance of the deviation are $(\bar{\delta},\sigma_\delta) = (-0.3,0.003)$ cm^{-1}.

22822 | *Phys. Chem. Chem. Phys.*, 2016, **18**, 22816–22826

This journal is © the Owner Societies 2016

Table 6 Rovibrational transitions assigned to the E^+ 35.7 cm^{-1} (J0.19–20) level of the zero-point vibration

No.	$J' \leftarrow J''$	Expt [MHz]	Expt [cm^{-1}]	$E(J')$ [cm^{-1}]	Label $(J')^a$	$E(J'')$ [cm^{-1}]	Label $(J'')^a$	Calc. [cm^{-1}]	δ^b [cm^{-1}]
Expt. (ref. 14): Table VII, E3, $\Sigma \leftarrow \Pi$ band									
1	1 ← 2	723657.8	24.1	36.0	J1.51–52	13.7	J2.15–16	22.3	1.8
2	2 ← 2	740443.2	24.7	36.5	J2.73–74	13.7	J2.15–16	22.9	1.8
3	1 ← 1	740778.1	24.7	36.0	J1.51–52	13.1	J1.15–16	22.9	1.8
4	0 ← 1	732385.1	24.4	35.7	J0.19–20	13.1	J1.15–16	22.6	1.8
5	2 ← 1	757561.5	25.3	36.5	J2.73–74	13.1	J1.15–16	23.4	1.8
Expt. (ref. 14): Table VII, E4, $\Delta \leftarrow \Pi$ band									
6	2 ← 2	821483.9	27.4	38.5	J2.88–89	13.7	J2.15–16	24.8	2.6
7	2 ← 1	838603.8	28.0	38.5	J2.88–89	13.1	J1.15–16	25.4	2.6
or:									
6	2 ← 2	821483.9	27.4	39.5	J2.90–91	13.7	J2.15–16	25.8	1.6
7	2 ← 1	838603.8	28.0	39.5	J2.90–91	13.1	J1.15–16	26.4	1.6
Expt. (ref. 14): Table VII, E5, $\Pi \leftarrow \Pi$ band									
8^c	2 ← 2	1057801.7	35.3	48.8	J2.116–117	13.7	J2.15–16	35.1	0.2
9^c	1 ← 1	1057943.1	35.3	48.2	J1.84–85	13.1	J1.15–16	35.1	0.2
10^c	2 ← 1	1074920.4	35.9	48.8	J2.116–117	13.1	J1.15–16	35.7	0.2

^{a} J$n.i$–j identifies the levels in the energy-level list provided in the ESI. ^{b} δ is the difference of the experimental and computed transitions. The mean and the sample variance of the deviation in the E3, E4, and E5 bands are $(\bar{\delta},\sigma_\delta)$ = (1.8,0.02) cm^{-1}, (1.6,0.002) cm^{-1}, and (0.2,0.004) cm^{-1}, respectively. The set of 1–5 transitions has the largest irregularities among all bands studied with a variance as large as 0.02 cm^{-1}. ^{c} The upper level in these transitions is assignable to the E^+ 48.2 cm^{-1} (J0.34–35) vibration.

Table 7 Rovibrational transitions assigned to the F_1^+ 4.8 cm^{-1} (J0.2–3) level of the zero-point vibration

No.	$J' \leftarrow J''$	Expt [MHz]	Expt [cm^{-1}]	$E(J')$ [cm^{-1}]	Label $(J')^a$	$E(J'')$ [cm^{-1}]	Label $(J'')^a$	Calc. [cm^{-1}]	δ^b [cm^{-1}]
Expt. (ref. 14): Table VIII, (A/F)5, $\Pi \leftarrow \Sigma$ band									
1	1 ← 2	827031.4	27.6	30.6	J1.38–43	5.6	J2.2–4	25.0	2.6
2	1 ← 1	844268.9	28.2	30.6	J1.38–43	5.0	J1.2–4	25.5	2.6
3	2 ← 2	844500.0	28.2	31.1	J2.48–53	5.6	J2.2–4	25.5	2.6
4	1 ← 0	852462.1	28.4	30.6	J1.38–43	4.8	J0.2–4	25.8	2.6
5	2 ← 1	860602.5	28.7	31.1	J2.48–53	5.0	J1.2–4	26.1	2.6

^{a} J$n.i$–j identifies the levels in the energy level list provided in the ESI. ^{b} δ is the difference of the experimental and computed transitions. The mean and the sample variance of the deviation are $(\bar{\delta},\sigma_\delta)$ = (2.6,0.01) cm^{-1}.

Table 8 Rovibrational transitions assigned to the F_2^+ 28.9 cm^{-1} (J0.9–11) and 36.3 cm^{-1} (J0.21–23) levels of the zero-point vibration

No.	$J' \leftarrow J''$	Expt [MHz]	Expt [cm^{-1}]	$E(J')$ [cm^{-1}]	Label $(J')^a$	$E(J'')$ [cm^{-1}]	Label $(J'')^a$	Calc. [cm^{-1}]	δ^b [cm^{-1}]
Expt. (ref. 14): Table IX, (A/F)6, $\Sigma \leftarrow \Pi$ band									
1	1 ← 2	889393.8	29.7	36.6	J1.53–55	8.5	J2.6–11	28.1	1.6
2	2 ← 2	906302.4	30.2	37.1	J2.75–77	8.5	J2.6–11	28.6	1.6
3	1 ← 1	906722.4	30.2	36.6	J1.53–55	7.9	J1.6–11	28.7	1.6
4	2 ← 1	924003.8	30.8	37.1	J2.75–77	7.9	J1.6–11	29.2	1.6
Expt. (ref. 14): Table IX, (A/F)7a, $\Delta \leftarrow \Pi$ band									
5	2 ← 2	912803.3	30.4	37.5	J2.80–85	8.5	J2.6–11	29.0	1.4
6	2 ← 1	930130.4	31.0	37.5	J2.80–85	7.9	J1.6–11	29.6	1.4
Expt. (ref. 14): Table IX, (A/F)7b, $\Delta \leftarrow \Pi$ band									
7	2 ← 2	912529.1	30.4	37.5	J2.80–85	8.5	J2.6–11	29.0	1.4
8	2 ← 1	930230.6	31.0	37.5	J2.80–85	7.9	J1.6–11	29.6	1.4

^{a} J$n.i$–j identifies the levels in the energy-level list provided in the ESI. ^{b} δ is the difference of the experimental and computed transitions. The mean and the sample variance of the deviation in the (A/F)6, (A/F)7a, and (A/F)7b, bands are $(\bar{\delta},\sigma_\delta)$ = (1.6,0.004) cm^{-1}, (1.4,0.003) cm^{-1}, and (1.4,0.005) cm^{-1}, respectively.

starting from the ZPV E^+ band *(vide infra)*. Anomalous $J' = 0 \leftarrow J'' = 1$ (and $J' = 1 \leftarrow J'' = 2$) rovibrational transitions are seen both in (the absorption) experiment and theory within the ZPV E^- (36.4 cm^{-1}, J0.24–25) and the ZPV F_1^- (32.6 cm^{-1}, J0.12–14; 32.7 cm^{-1}, J0.15–17) bands of the 'ortho' species and within the ZPV E^+(35.7 cm^{-1}, J0.19–20) and the ZPV F_2^+ (28.9 cm^{-1}, J0.9–11; 36.3 cm^{-1}, J0.21–23) bands of the 'para' species.

The assignment of the vibrational bands and most rovibrational levels is unambiguous; however, due to the near symmetric prolate character of the complex there are nearly degenerate levels, which cannot be unambiguously assigned based on the computations. This ambiguity could be eliminated if there was an exceedingly accurate potential energy surface available, which could be used to obtain a rovibrational energy level ordering resolved to better than

Table 9 Rovibrational transitions assigned to the A_1^+ 0.0 cm^{-1} (J0.1) level of the zero-point vibration

No.	$J' \leftarrow J''$	Expt [MHz]	Expt [cm^{-1}]	$E(J')$ [cm^{-1}]	Label $(J')^a$	$E(J'')$ [cm^{-1}]	Label $(J'')^a$	Calc. [cm^{-1}]	δ^b [cm^{-1}]
Expt. (ref. 14): Table X, (A/F)8 $\Pi \leftarrow \Sigma$ band
1	$1 \leftarrow 2$	901595.6	30.1	29.4	J1.30–31	0.9	J2.1	28.6	1.5
2	$1 \leftarrow 1$	919166.0	30.7	29.4	J1.30–31	0.3	J1.1	29.1	1.5
3	$2 \leftarrow 2$	919232.4	30.7	30.0	J2.40–41	0.9	J2.1	29.1	1.5
4	$1 \leftarrow 0$	927673.3	30.9	29.4	J1.30–31	0.0	J0.1	29.4	1.5
5	$2 \leftarrow 1$	936059.3	31.2	30.0	J2.40–41	0.3	J1.1	29.7	1.5

^{a} J$n.i$–j identifies the levels in the energy-level list provided in the ESI. ^{b} δ is the difference of the experimental and computed transitions. The mean and the sample variance of the deviation are $(\bar{\delta}, \sigma_\delta) = (1.5, 0.007)$ cm^{-1}.

0.5 cm^{-1} (which is perhaps even beyond the accuracy of the common Born–Oppenheimer[32] and non-relativistic approximations[33]). In lieu of a fully resolved list, we assign a rovibrational transition to a sub-manifold of upper and/or lower rovibrational levels (see Fig. 5 and 6), without attempting to make a definitive decision about these non-strictly-degenerate but very-close-lying levels. In these cases, we computed the transition energy as the difference between the centers (energy averages) of the upper and lower sub-manifolds (Tables 2–9). Apart from these very small effects, we can confirm that the rovibrational transitions within a single band have a systematic error (experiment−theory) with an exceedingly small variance, which is on the order of the energy difference of the nearly degenerate levels.

Detailed comparison of the computed and measured rovibrational transitions within the eight experimentally studied main bands (occasionally with a few sub-bands)[14] is provided in Tables 2–9. The mean and the variance of the deviation of experiment and theory is around (2,0.01) cm^{-1} and (0.5,0.005) cm^{-1} for the *para* and for the *ortho* species, respectively. In general, the agreement and the consistency (the mean and the variance of the deviation) between experiment and theory is better for the *ortho* species. A possible contributor to the cause of this difference is the 3 : 1 ratio of the spin-statistical weights and of the corresponding transition intensities.

The largest discrepancies between experiment and theory are observed for the 1–5 rovibrational transitions of the E$^+$ vibration (Table 6). For the 6–7 transitions of this band (Table 6), we cannot decide unambiguously between two possible upper states, with energies 38.5 cm^{-1} and 39.5 cm^{-1}. Comparing the systematic error of the computed transitions with the error of the 1–5 transitions, it seems more likely that the upper level of the 6–7 transitions is the one with an energy of 38.5 cm^{-1}. The systematic error of the 8–10 transitions (Table 6) is markedly different from the error of the 1–5 transitions. This deviation is explained by the fact that the upper levels of the 8–10 transitions do not belong to the ZPV(GM) splitting manifold, but they are the $J = 1$ and $J = 2$ rotational excitations of the E$^+$ 48.2 cm^{-1} (J0.34–35) vibration.

Most importantly, all experimentally reported transitions[14] within the $J = 0, 1, 2$ manifold are identified in our variationally computed dataset. For the *ortho* species (see Fig. 5), all levels within the computed ZPV(GM) manifold (up to $J = 2$) are involved in at least one experimentally reported transition. For the *para* species (see Fig. 6), however, there are a few computed levels within the ZPV(GM) manifold (up to $J = 2$) that are not involved in any experimentally reported transitions

Table 10 Computed rovibrational energy levels assigned to the ZPV(GM) manifold, which could be observed *via* rovibrational transitions within the same energy range as the experiments of ref. 14 were performed (E_0 is the lowest vibrational energy)

Vibrational band	J	$E - E_0$ [cm^{-1}]	Label
E$^+$ (35.7 cm^{-1}, J0.19–20)	1	38.9	J1.58–59
	2	39.5	J2.90–91
F$_1^+$ (4.8 cm^{-1}, J0.2–4)	2	40.9	J2.92–97
F$_2^+$ (28.9 cm^{-1}, J0.9–11) & F$_2^+$	0	28.9	J0.9–11
(36.3 cm^{-1}, J0.21–23)	0	36.3	J0.21–23
	1	29.2	J1.27–29
	2	29.8	J2.37–39

(there are no arrows starting from or pointing to these levels indicated with a solid line in the figures). These theoretically predicted levels of the ZPV(GM) rovibrational manifold are listed in Table 10 and are awaiting experimental confirmation.

There are also energy levels labeled with a dashed line in Fig. 5 and 6. These levels have a strongly mixed RRD with some minor contribution from the ZPV(GM) vibrational band in which they are shown. We indicated these levels in the figures because they could be observed in transitions under similar conditions as in ref. 14. Furthermore, by counting all energy levels and by including these strongly mixed ones, *i.e.*, summing all (n) values shown next to the (solid or dashed) lines in each rovibrational band, we obtain $2J + 1$ rovibrational levels in total, except for the ZPV A$_1^+$ (0.0 cm^{-1}, J0.1) with $J = 2$. In that case two additional rovibrational levels should appear with rovibrational energies ($J = 2$) larger than 54.9 cm^{-1}, *i.e.*, beyond the first 150 energy levels which were computed.

Finally, transitions between the rovibrational levels of the ZPV(GM), A$_1^+$ (0.0 cm^{-1}, J0.1), and the lowest-lying levels of the ZPV manifold of the secondary minimum, ZPV(SM), A$_1^+$ (34.4 cm^{-1}, J0.18), could be identified in the experimental spectra, because these transitions lie within the same energy range as the transitions reported in ref. 14. The predicted levels of the secondary minimum,

Table 11 Computed rovibrational energy levels of the ground-state vibration of the secondary minimum, which could be observed *via* rovibrational transitions within the same energy range as the experiments of ref. 14 were performed (E_0 is the lowest vibrational energy)

Vibrational band	J	$E - E_0$ [cm^{-1}]	Label
A$_1^+$ (34.4 cm^{-1}, J0.18)	1	34.7	J1.50
	1	59.3	J1.134–135
	2	35.2	J2.72

22824 | *Phys. Chem. Chem. Phys.*, 2016, **18**, 22816–22826

This journal is © the Owner Societies 2016

which could potentially be observed as upper levels in rovibrational transitions, are listed in Table 11. Locating such transitions would constitute the first experimental confirmation for the existence of a secondary minimum in the methane–water complex, where the methane molecule is the proton donor and the water molecule is the proton acceptor.

4 Summary and conclusions

We have computed rovibrational energy levels for the methane–water dimer corresponding to an accurate potential energy surface developed by Akin-Ojo and Szalewicz[15]. The computations exploited the capabilities of the fourth generation[34] quantum chemical code GENIUSH[16,17]. After a careful analysis of the computed states, excellent, quantitative agreement is obtained between the calculated and experimentally reported far-infrared[14] transitions of this complex, which were previously left unassigned. This excellent agreement suggests that the dimer interaction potential energy surfaces available for $CH_4 \cdot H_2O^{6,15}$ can be used with confidence and their combination with the three-body methane–water–water[7] (and the corresponding two- and three-body water–water interaction surfaces[3–5]) opens up new avenues for the study of larger clusters[10] and bulk-phase properties of methane–water mixtures.

Concerning the fine details of the rovibrational spectroscopy of the methane–water dimer, all experimentally reported transitions within the $J = 0$, 1, 2 rovibrational manifold are identified in our computations. They are assigned to rovibrational energy levels corresponding to the 24-member zero-point vibrational (ZPV) manifold of the global minimum (GM) structure (in which the water molecule is the proton donor and the methane molecule is the acceptor). The exceptions are three transitions whose upper level is higher in energy than the ZPV(GM) manifold. We identified a few rovibrational levels in the computed ZPV(GM) rovibrational splitting manifold, which lie in the same energy range, and thus could potentially be observed under the same experimental conditions, but were not reported in ref. 14.

We have also identified (ro)vibrational energy levels that could only be assigned to the secondary minimum (SM) of the complex, in which the methane molecule is the proton donor and the water molecule is the acceptor. The lower part of the 24-member ZPV(SM) manifold overlaps the upper part of the 24-member ZPV(GM) set; hence, rovibrational transitions ending in levels corresponding to the secondary minimum well might be observed in the same energy range as the transitions reported in ref. 14.

Anomalous, reversed rovibrational-energy level ordering, *i.e.*, negative rotational excitation energy, is observed both in the experimental and in the computed transitions. This observation provides additional confirmation of the excellent agreement between theory and experiment, and, furthermore, indicates that this extremely floppy, astructural[19,22] complex exhibits rich internal quantum dynamics, suggesting that further experimental and theoretical work will be worth pursuing both from fundamental and applied research perspectives.

References

1 J. N. Murrell, S. Carter, S. C. Farantos, P. Huxley and A. J. C. Varandas, *Molecular Potential Energy Functions*, Wiley, New York, 1984.

2 B. J. Braams and J. M. Bowman, *Int. Rev. Phys. Chem.*, 2009, **28**, 577.

3 Y. Wang and J. M. Bowman, *J. Chem. Phys.*, 2011, **134**, 154510.

4 G. R. Medders, V. Babin and F. Paesani, *J. Chem. Theory Comput.*, 2013, **9**, 1103.

5 V. Babin, G. R. Medders and F. Paesani, *J. Chem. Theory Comput.*, 2014, **10**, 1599.

6 C. Qu, R. Conte, P. L. Houston and J. M. Bowman, *Phys. Chem. Chem. Phys.*, 2015, **17**, 8172.

7 R. Conte, C. Qu and J. M. Bowman, *J. Chem. Theory Comput.*, 2015, **11**, 1631.

8 T. S. Collett, A. H. Johnson, C. C. Knapp and R. Boswell, Natural Gas Hydrates: A Review, in *Natural gas hydrates–Energy resource potential and associated geologic hazards*, ed. T. S. Collett, A. H. Johnson, C. C. Knapp and R. Boswell, AAPG/NETL/AAPG Foundation/AAPG EMD, 2010, vol. M 89, pp. 146–219.

9 E. Dartois and D. Deboffle, *Astron. Astrophys.*, 2008, **490**, L19.

10 C. Qu and J. M. Bowman, *J. Phys. Chem. C*, 2016, **120**, 3167.

11 A. K. Sum, R. C. Burruss and E. D. Sloan, *J. Phys. Chem. B*, 1997, **101**, 7371.

12 H. Ohno, M. Kida, T. Sakurai, Y. Iizuka, T. Hondoh, H. Narita and J. Nagao, *ChemPhysChem*, 2010, **11**, 3070.

13 R. D. Suenram, G. T. Fraser, F. J. Lovas and Y. Kawashima, *J. Chem. Phys.*, 1994, **101**, 7230.

14 L. Dore, R. C. Cohen, C. A. Schmuttenmaer, K. L. Busarow, M. J. Elrod, J. G. Loeser and R. J. Saykally, *J. Chem. Phys.*, 1994, **100**, 863.

15 O. Akin-Ojo and K. Szalewicz, *J. Chem. Phys.*, 2005, **123**, 134311.

16 E. Mátyus, G. Czakó and A. G. Császár, *J. Chem. Phys.*, 2009, **130**, 134112.

17 C. Fábri, E. Mátyus and A. G. Császár, *J. Chem. Phys.*, 2011, **134**, 074105.

18 E. Mátyus, C. Fábri, T. Szidarovszky, G. Czakó, W. D. Allen and A. G. Császár, *J. Chem. Phys.*, 2010, **133**, 034113.

19 J. Sarka and A. G. Császár, *J. Chem. Phys.*, 2016, **144**, 154309.

20 C. Fábri, E. Mátyus and A. G. Császár, *Spectrochim. Acta*, 2014, **119**, 84–89.

21 C. Fábri, A. G. Császár and G. Czakó, *J. Phys. Chem. A*, 2013, **117**, 6975.

22 C. Fábri, J. Sarka and A. G. Császár, *J. Chem. Phys.*, 2014, **140**, 051101.

This journal is © the Owner Societies 2016

Phys. Chem. Chem. Phys., 2016, **18**, 22816–22826 | **22825**

23 K. Kuchitsu and L. S. Bartell, *J. Chem. Phys.*, 1962, **36**, 2460.

24 G. Czakó, E. Mátyus and A. G. Császár, *J. Phys. Chem. A*, 2009, **113**, 11665.

25 M. Nakata and K. Kuchitsu, *J. Chem. Soc. Jpn.*, 1986, 1446.

26 E. Cohen, T. Cvitaš, J. Frey, B. Holmström, K. Kuchitsu, R. Marquardt, I. Mills, F. Pavese, M. Quack, J. Stohner, H. Strauss, M. Takami and A. Thor, *Quantities, Units and Symbols in Physical Chemistry (the IUPAC Green Book – 3rd edition)*, RSC Publishing, Cambridge, 2007.

27 D. J. Wales, *OPTIM: A program for geometry optimisation and pathway calculations*, http://www-wales.ch.cam.ac.uk/software.html.

28 L. J. Munro and D. J. Wales, *Phys. Rev. B: Condens. Matter Mater. Phys.*, 1999, **59**, 3969–3980.

29 T. R. Dyke, *J. Chem. Phys.*, 1977, **66**, 492.

30 V. Szalay, A. G. Császár and M. L. Senent, *J. Chem. Phys.*, 2002, **117**, 6489.

31 Y. Ohshima and Y. Endo, *J. Chem. Phys.*, 1990, **93**, 6256.

32 E. Mátyus and M. Reiher, *J. Chem. Phys.*, 2012, **137**, 024104.

33 O. L. Polyansky, A. G. Császár, S. V. Shirin, N. F. Zobov, P. Barletta, J. Tennyson, D. W. Schwenke and P. J. Knowles, *Science*, 2003, **299**, 539.

34 A. G. Császár, C. Fábri, T. Szidarovszky, E. Mátyus, T. Furtenbacher and G. Czakó, *Phys. Chem. Chem. Phys.*, 2012, **14**, 1085.